



Identification of coronary arteries in CT images by Bayesian analysis of geometric relations among anatomical landmarks

Byunghwan Jeon ^{a,b}, Yeonggul Jang ^{a,b}, Hackjoon Shim ^{b,d,*}, Hyuk-Jae Chang ^{b,c}

^a Brain Korea 21 Project for Medical Science, Yonsei University, Seoul, Republic of Korea

^b Cardio-vascular ICT Research Center, Seoul, Republic of Korea

^c Division of Cardiology, Severance Cardiovascular Hospital, Yonsei University College of Medicine, Seoul, Republic of Korea

^d Cardiovascular Research Institute, Yonsei University College of Medicine, Republic of Korea

ARTICLE INFO

Article history:

Received 12 September 2018

Revised 9 June 2019

Accepted 7 July 2019

Available online 8 July 2019

Keywords:

Computed tomography angiography

Bayesian

Localization

Coronary artery

Multiple target

Curve analysis

Curvature and torsion

ABSTRACT

We propose a robust method for the identification of coronary arteries in computed tomography angiography (CTA) images. Utilizing geometric relations among the target and reference objects, which are assumed to follow a Gaussian distribution, an anatomic and geometric model is designed by Bayesian inference, which provides robust geometric priors for the target object localization. As a prerequisite process for the identification of coronary arteries, partially broken coronary artery segments found in CTA images are grouped and reconnected by geometric analysis of higher order curves connecting the broken segments. The geometric properties such as curvature and torsion represent naturalness and consistency between the vessel segments. As a problem to identify coronary arteries from CTA images, we demonstrate the robustness and accuracy of the proposed method in comparison with existing methods including commercial workstations on a variety of CTA cases.

© 2019 Elsevier Ltd. All rights reserved.

1. Introduction

Cardiovascular diseases (CVDs) are the leading cause of death in the world [1]. Localization of anatomical structures is a prerequisite process for most tasks in the assessment of CVDs. Coronary arteries, as one of the main causes of CVDs, are thin and curvilinear structures. Identification of the coronary arteries is addressed with the method proposed herein. First, robust detection of the three main coronary arteries (right coronary artery, RCA; left anterior descending artery, LAD; and left circumflex artery, LCX) is required for automatic extraction of the tree structure, precise lumen and/or wall boundaries, or other applications.

Abbreviations: AA, ascending aorta; CCA, connected component analysis; CTA, computed tomography angiography; CTO, chronic total occlusion; CVD, cardiovascular disease; DA, descending aorta; FN, false negative; FOV, field of view; FP, false positive; FPR, false positive rate; GT, ground truth; LA, left atrium; LAA, left atrial appendage; LAD, left anterior descending artery; LCA, left coronary artery; LCX, left circumflex artery; LGM, local geometric method; MSL, marginal space learning; OP, outermost point; RCA, right coronary artery; ROC, receiver operating characteristic; ROI, region of interest; TN, true negative; TP, true positive; FP, false positive; FN, false negative; TPR, true positive rate.

* Corresponding author at: #201, 543, Seongsan-ro, Seodaemun-gu, Seoul, Republic of Korea.

E-mail addresses: byunghwanjeon@yonsei.ac.kr (B. Jeon), jyg1722@gmail.com (Y. Jang), hjshim@yuhs.ac (H. Shim), hjchang@yuhs.ac (H.-J. Chang).

Analysis and detection of elongated structures in three-dimensional (3D) CTA images is a challenging task. The difficulty arises from both the sparsity of the images and complex geometry with irregularly shaped bifurcations. Such structures are naturally fragile, and their contours can be disrupted by even a small amount of noise. When the subject of the problem to be solved is the coronary artery, the physical effects due to the motion or lesion are further exacerbated, which leads to disconnections or misconnections. Ascending aorta and coronary arteries found in a real CTA image are shown in Fig. 1.

Many approaches to coronary seed detection consider only coronary ostia as starting points for tracking methods. Yang et al. [2] first found the ascending aorta using a Hough transform on axial images and then used ray casting to search for the two ostium points within angle constraints. Zheng et al. [3] proposed a method for finding the coronary ostia using the prior distribution of ostia on the surface of the aorta learned from a training set. Wang and Smedby [4] found the largest components around the aorta to use as the coronary seeds. The model-driven approach [5] registers the mean coronary model to the pre-detected heart chambers and coronary ostia. Gulsun et al. used a simple convolutional neural network to prune false positive branches to increase the accuracy [6]. However, the above approaches depend on the detection methods of chambers and coronary ostia. Further, distal parts of broken blood vessels cannot be detected.

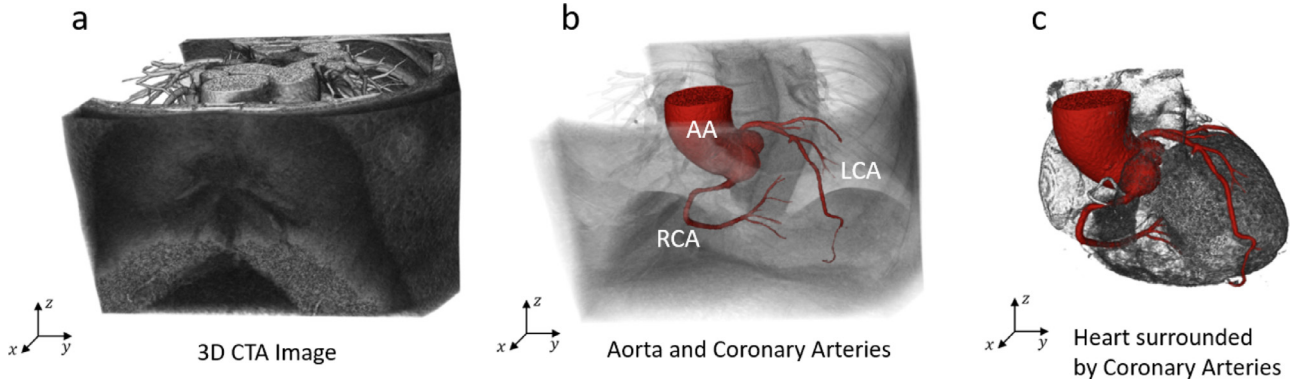


Fig. 1. Volume rendering of CTA image (grey) and regions of aorta and coronary artery (red): (a) cardiac CTA volume images that contain not only a heart but also other vessels and organs, (b) region of ascending aorta, AA and coronary artery, RCA and LCA (red), (c) a heart region (grey) and GT (red). (For interpretation of the references to color in this figure legend, the reader is referred to the web version of this article.)

While these approaches are based on the fact that a coronary artery is connected to the ascending aorta, there are some approaches that detect the middle part of the coronary artery directly by using local features [7,8]. These direct detection approaches have an advantage that they can detect blood vessels with severe lesions. In the case of chronic total occlusion (CTO) vessels, owing to the lack of contrast and the structure of broken blood vessels, the coronary tracker can be diverted elsewhere or terminate. Even though some approaches based on the optimized path between two points [9–11] may be sufficiently robust for the extraction of CTO vessels, they require the manual identification of the start point and the end point.

A topological approach [12] finds local maxima for blood vessels and then performs connected component analysis to label the 3D candidates. Final selection of coronary artery requires manual placement of a point. The approach has a potential to be improved by combining vesselness filtering methods. The vesselness filter [13] based on the Hessian matrix is widely used. There is a recently introduced method [14] to characterize curvilinear structures by ROPRPO (ranking the orientation responses of path operators), which can enhance the intensity features on vessel-like structures. Furthermore, automatic selection and geometrical analysis for grouping small vessel-like objects and classifying among true branches and false positives are considered for making the approach fully automated.

A survey paper on curvilinear object segmentation [15] in multiple applications presented two-dimensional (2D)-based approaches to retinal vessel segmentation, where the curvature property for 2D curvilinear structures is used as one of the important features [16–19]. However, the torsion property of 3D vessels is rarely used in spite of its important in 3D curvilinear structures. We analyzed the geometric properties including torsion to calculate the consistency between any pair of broken blood vessels.

We recently introduced a pairwise estimator [20] for the localization of two aortas or ostia of the coronary artery using geometric relations. The method uses distance and angle with the x-axis of the axial image between the two most circular objects. The left and right coronary arteries connected to the ascending aorta are also considered as two targets, and the proximal regions for the two targets are identified. The results show that the geometric relations of the cardiac anatomical landmarks can be utilized as robust prior information.

In this paper, we propose a new expanded method to identify target objects automatically, the features of which are difficult to define, based on the locations of at least two robust reference objects. As an application of the method, fully automatic identification of coronary arteries in CT images is proposed. In order to

Table 1

The constant distance and angle parameters between two target objects as optimal parameters for identification of coronary artery.

Reference	RCA (mm)		LAD (mm)		LCX (mm)	
	μ	σ	μ	σ	μ	σ
AA	34.53	7.19	87.50	10.65	74.90	7.87
DA	118.58	13.79	131.00	14.95	54.23	22.50

μ : average distance, σ : deviation where $\mu = \frac{1}{n} \sum_{i=1}^n \delta_i$, $\sigma = \sqrt{\frac{\sum_{i=1}^n (\mu - \delta_i)^2}{n-1}}$. Values μ and σ are directly used for computing Eq. (4) as optimal parameters. AA, ascending aorta; DA, descending aorta; RCA, right coronary artery; LAD, left anterior descending coronary artery; LCX, left circumflex artery.

optimize the identification, we also proposed a method for reconnecting vessels, which are easily broken with coronary diseases or motion artifacts, using higher-order analysis.

In the beginning, all the vessel-like candidates are prepared through filtering, labeling, and connecting based on geometric analysis. Then, a Bayesian inference approach that is optimized for coronary artery directly identifies coronary arteries by using the relations among reference and target objects.

2. Method

The sizes or lengths of any parts of the heart can be statistically represented with two parameters, viz., the mean and the standard deviation [21]. Our assumption is that the relative lengths and sizes among different parts also follow a Gaussian distribution; hence, we estimated the geometric relations using the mean and standard deviation obtained from a public dataset [22,23], as given in Table 1. The proposed method estimates multiple target objects based on the cardiac geometric relations modeled as in Fig. 2. The outermost point (OP) is the farthest point from the inside of the heart, which is also described based on the real CTA image in Section 3.1.

We use these geometric relations as prior distributions to detect the positions of the target objects. Cross-sections of ascending and descending aortas are found robustly and used as two references in cardiac CTA images. The location of the target object is simply specified by computing the distance-based geometric relations among reference and target objects. Bayesian inference is appropriate for modeling geometric relations in the heart, taking into account variations in cardiac size and measuring the features of target objects. The details of a Bayesian formula are given in Section 2.3.

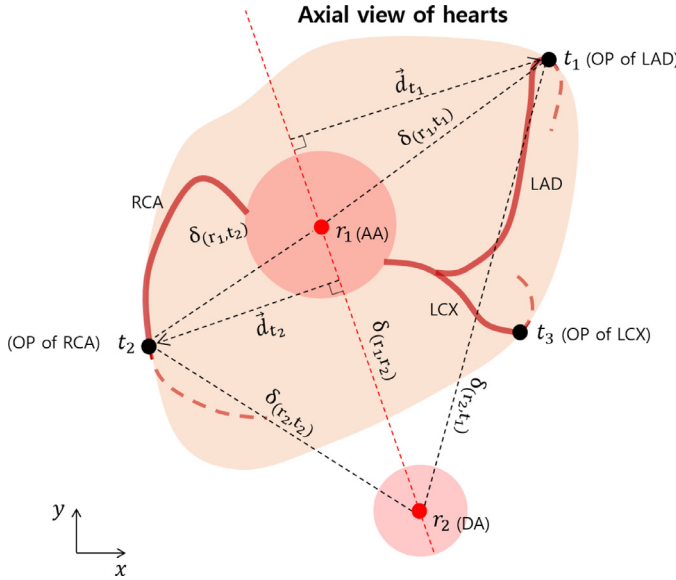


Fig. 2. A geometric model for the relationship of two reference objects (AA, DA) and three target objects (OPs of LAD, LCX, and RCA). r and t are the centroids of the reference objects and target objects, respectively. δ is the distance between r and t , and \vec{d} is a vector that is perpendicular to the line passing through the centroids of the reference objects and toward the target t . The positions of the targets can be described statistically based on the positions of the reference objects. (AA: ascending aorta, DA: descending aorta, OP: outermost point, LAD: left anterior descending artery, LCX: left circumflex artery, RCA: right coronary artery).

We denote the target candidate set as $\mathcal{T} = \{t_i \mid 1 \leq i \leq N_T\}$ and reference object set as $\mathcal{R} = \{r_j \mid 1 \leq j \leq N_R\}$ in a cardiac CTA image. Note that t_i and r_j in sets \mathcal{T} and \mathcal{R} are either a voxel or a region of interest (ROI) depending on the preprocessing method that will be described in detail in Sections 2.1 and 2.2, respectively. Connected component analysis (CCA) is applied as a preprocessing step to cluster and label each connected component in image intensity I or vesselness map V that is an eigenvalue map of Hessian matrix of I . The geometric relation between set \mathcal{T} and \mathcal{R} is described in Fig. 2.

2.1. Preparation of reference objects \mathcal{R} in cardiac CTA

Detecting the locations of the aortas is usually a prerequisite for coronary segmentation, and aortas have the relatively distinct features of large, thick, stem-like shapes and the appearance of two large circles in the axial view. For these reasons, ascending and de-

scending aortas (AA and DA, respectively) are chosen as reference objects ($N_R = 2$). Many approaches to the detection of aortas have already been introduced based on Hough circle transform [24,25]. By using these methods, two circular shapes should be found independently. However, if one of the aortas cannot be found, it cannot be used as a robust reference.

Our alternative is to find the locations of the two aortic cross-sections simultaneously via a method [20] that exploits the ratios of the eigenvalues from the covariance matrix Σ_{r_i} . There are geometric anatomic relations with angles θ and distances δ between the two aortas. By this method, we can obtain two 3D lines passing through the aortic centers.

To detect 3D target regions, two reference locations, the centroids of the AA and DA, should exist in all 2D (x , y) planes. The two straight lines r_1 , r_2 passing through the centroids in the major directions of AA and DA, are found respectively, as shown in Fig. 3. $r_{1,z}$ and $r_{2,z}$ would be the two reference objects in the x - y 2D planes covering the entire range of z values.

2.2. Preparation of target objects \mathcal{T} in cardiac CTA

All the curvilinear objects in CT images are considered candidates of coronary arteries for our approach, and the candidates can be simply prepared according to the following description. Input CTA images are linearly interpolated to acquire isotropic volumes. To remove pulmonary vessels (PVs), we use the simple morphological operator having a spherical kernel of eight voxel radius introduced in [2]. Then, a vesselness map V (Fig. 5(b)) is obtained from I using a multiscale vesselness filter [13]. All the vessel-like objects in the vesselness map V are labeled by CCA. Then, the set of the labeled vessel-like segments $\mathcal{T} = \{t_i \mid 1 \leq i \leq N_T\}$, $\mathcal{T} \subseteq \mathbb{R}^3$, is obtained. The initial candidate set \mathcal{T} can be optimized by the reconnecting and grouping method introduced in the Section 2.4. Our goal is to identify the one segment maximizing the posterior probability of Eq. (2) among the N_T candidates, and this will be the target object (RCA, LAD, or LCX) (Fig. 5(e),(f)).

In the case shown in Fig. 4(a), for example, there are 128 candidates; The cross-sectional diameter $\phi_i(p)$ of a candidate t_i is important because the main coronary arteries of interest (Fig. 4 (b)) are thicker than other blood vessels (Fig. 4 (c), (d)) in the heart, so the larger the diameter, the higher is the probability of the candidate.

2.3. Maximum a posteriori estimation

Coronary arteries transport blood into cardiac muscles. Therefore, the directions in which the coronary arteries stretch from AA

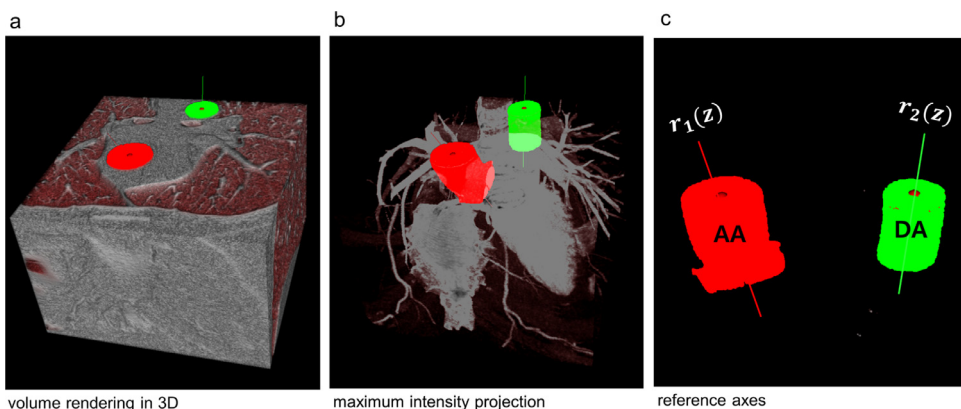


Fig. 3. (a) The detected references are visualized on the axial side of the volume. (b) Each of two cylinder-like objects is approximated with a 3D line to cover the entire range of the volume. Once two reference lines are detected, (c) They are very useful in that the position of any object in 3D computed tomography angiography (CTA) images can be specified by the positions of the two references.

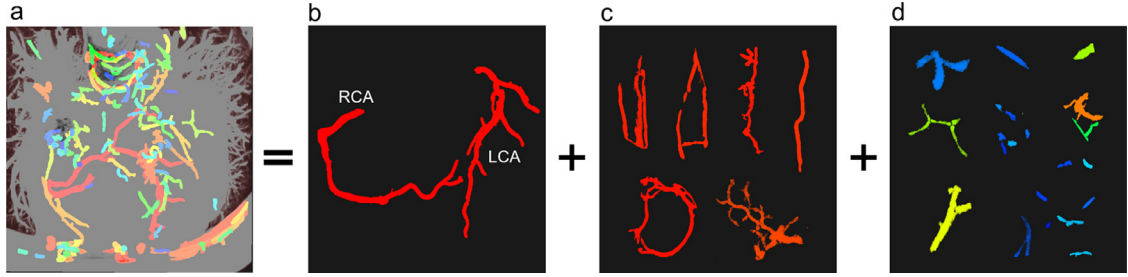


Fig. 4. The division of all labeled vessel-like candidates into three classes. (a) 3D volume rendering of all of the labeled vessel-like objects \mathcal{T} . (b) Coronary arteries (RCA and LCA) have the largest of diameter among the object in most cases. These two objects are the targets in this case. (c) Other objects that are not coronary arteries. (d) Meaningless fragments caused by noise or artifacts.

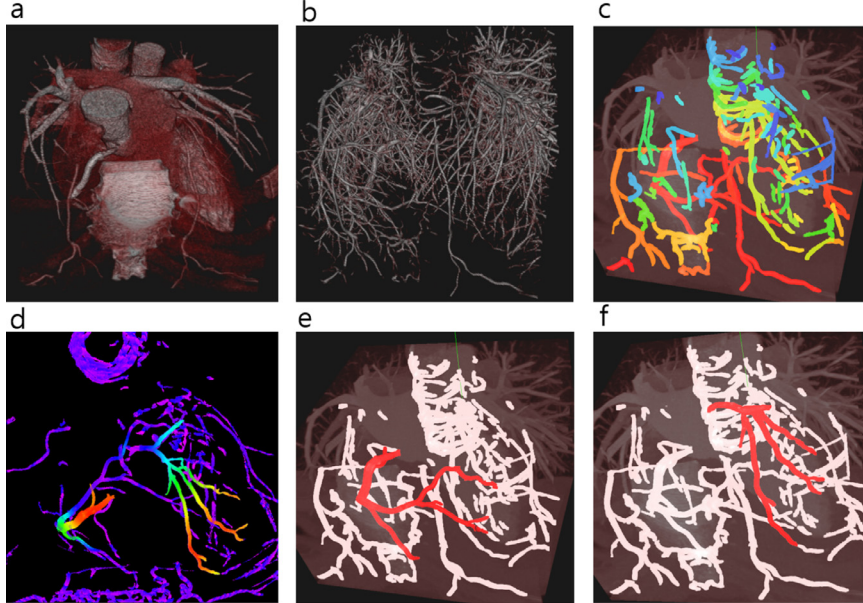


Fig. 5. The process for coronary artery identification. (a) The original image I . (b) The vesselness map V found by applying the method in [13] to I . (c) Connected component analysis (CCA) is applied to V , grouping and labeling all the vessel-like objects in the volume as candidates for the main coronary artery. (d) The average color map of the posterior probability (Eq. (1)) on the vessel-like candidates for the selection of one target segment. (e) The highest posterior probability on the right coronary artery (RCA) segment. (f) The highest posterior probability on the left coronary artery (LCA) segment.

are quite clear, and their positional variations are small. The relative distances of OPs of RCA, LAD, and LCX from the patient's aortas (AA and DA), which represent the geometric relations, are collected from several public datasets [22,23] and estimated as μ and σ . We want to combine these geometric relations with the vesselness probability, and the patient's cardiac size is adjusted using the distance between the two aortic cross-sections.

Our rationale behind the proposed approach to identifying the three main coronary arteries (RCA, LAD, and LCX) is based on the following characteristics:

1. Coronary arteries are filled with a contrast agent and have specific attenuation values.
2. There are specific geometric relations between the coronary arteries and the two ascending and descending aortic cross-sections.
3. The three coronary arteries are larger than the surrounding vessels in diameter.

We introduce a complete process for finding the main coronary arteries (Fig. 5) that reflects these characteristics. The process is divided into two main steps. First, all of the 3D vessel-like objects in the CTA images are segmented by CCA in a vesselness map and the grouping method, which is described in Sections 2.1 and 2.2. Sec-

ond, the target object is estimated via a Bayesian formula (Eqs. (1)–(7)) using the geometric relations to the detected reference objects.

We have the following Bayesian formula, given reference and target candidates \mathcal{R} , \mathcal{T} and CT image I :

$$\begin{aligned}
 P(t_i | I, V, \mathcal{R}) &= P(t_i | I, \mathcal{R}) \\
 &= \prod_{z=1}^{N_z} P(t_{i,z} | I, \mathcal{R}) \\
 &\propto \prod_{z=1}^{N_z} P(I, \mathcal{R} | t_{i,z}) \cdot P(t_{i,z}) \\
 &= \prod_{z=1}^{N_z} \{P(I | t_{i,z}) P(\mathcal{R} | t_{i,z}) \cdot P(t_{i,z})\} \\
 &= \prod_{z=1}^{N_z} \{P(I | t_{i,z}) \prod_{j=1}^{N_R} P(r_j | t_{i,z}) \cdot P(t_{i,z})\}
 \end{aligned} \tag{1}$$

where I , V , and \mathcal{R} are the CTA image, its vesselness map, and the set of reference objects, respectively. We drop $P(I)$ and $P(\mathcal{R})$ terms because they are constants with respect to the optimization parameters. 3D object t_i can be expressed as a union of the 2D objects on multiple slices $t_i = \bigcup_{z=1}^{N_z} t_{i,z}$. 2D planes normal to the z -axis in a 3D CTA image are referred to as a typical diag-

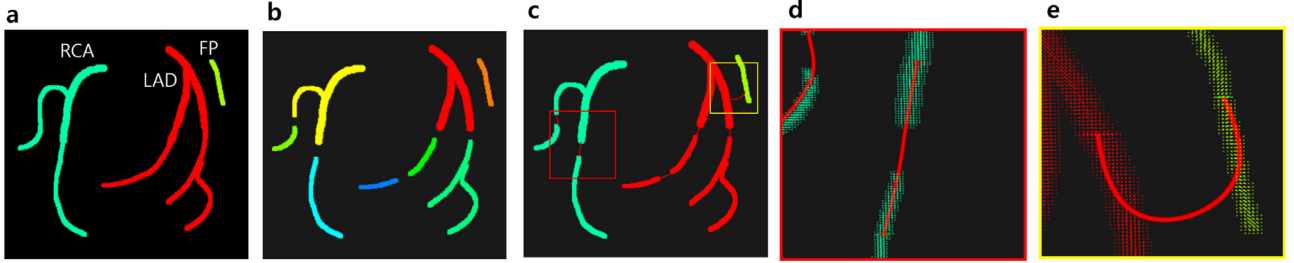


Fig. 6. Illustration of disconnected coronary segments in a synthetic example. (a) unbroken normal vessel (b) severely broken vessel : eight initial segments ($|T|=8$) are labeled by CCA., (c) after grouping of the segments through geometric analysis, eight segments are merged into three segments ($|T|=3$), which is the final candidate T for the target estimator in Eq. (6)., (d) a connecting curve with small curvatures, (e) a connecting curve with higher curvatures.

nostic view, clinically defined as an axial view. Eq. (1) is modeled to take the important advantages of the axial view. Two ascending and descending aortas have circular shapes in the axial view, and they can be utilized as a robust reference for \mathcal{R} . $P(I|t_{i,z})$ is the likelihood, a probability decided only by the image data, and $\prod_{j=1}^{N_R} P(r_j|t_{i,z}) \cdot P(t_{i,z})$ act as priors, because they use pre-measured geometric relations or diameter of the coronary artery. Then, the target objects are estimated by maximizing this a posteriori probability in Eq. (2).

In essence, the maximum a posteriori estimator aims to estimate the relations between the reference object \mathcal{R} and the target object T based on the 2D plane normal to the z -axis, and finally the 3D target object is estimated.

$$\begin{aligned} & \operatorname{argmax}_i \prod_{z=1}^{N_z} \{P(I|t_{i,z})\} \prod_{j=1}^{N_R} P(r_j|t_{i,z}) \cdot P(t_{i,z}) \\ & = \operatorname{argmax}_i \sum_{z=1}^{N_z} \{L(I|t_{i,z}) + \sum_{j=1}^{N_R} L(r_j|t_{i,z}) + L(t_{i,z})\}, \end{aligned} \quad (2)$$

where $L(\cdot)$ is the log-likelihood: $L(\cdot) = \log P(\cdot)$.

We model the posterior probability using the geometric model shown in Fig. 2 to identify the coronary arteries among a large number of candidates. Recall that in the Bayesian inference in Eq. (2), two major terms are derived, representing pure data and prior knowledge of the geometric relations. The former, the likelihood $L(I|t_{i,z})$, is modeled for contrast enhancement. The latter, the prior $L(\mathcal{R}|t_{i,z}) + L(t_{i,z})$, is divided again into two terms: $L(\mathcal{R}|t_{i,z})$ is modeling for anatomic geometric relations among the reference and target objects, and $L(t_{i,z})$ is derived from the diameter of $t_{i,z}$. The prior $L(\mathcal{R}|t_{i,z})$ is called the geometric prior.

Likelihood reflects coronary arteries with contrast attenuation:

$$L(I|t_{i,z}) = -\frac{|\mu_C - I(p)|^2}{\sigma_C^2} \quad (3)$$

where $p \in t_i$ and $I(p)$ is an intensity value on a point p . μ_C and σ_C for the contrast are estimated from several CTA images, a process that is introduced in detail in the next section.

Geometric prior $L(\mathcal{R}|t_{i,z})$ is a probabilistic representation of a geometric relation that takes into account the distance between at least two reference objects and the target object to specify a target region:

$$L(\mathcal{R}|t_{i,z}) = \sum_{j=1}^{N_R} L(r_j|t_{i,z}) = -\sum_{j=1}^{N_R} \left\{ \frac{|\mu_{r_j,t_{i,z}} - \lambda \cdot \delta_{r_j,t_{i,z}}|^2}{\sigma_{r_j,t_i}^2} \right\} \quad (4)$$

where δ is the distance between a reference and a target as described in Fig. 2. μ and σ are average of δ and its deviation, respectively, as described in Table 6, and $\lambda = (\mu_{r_1,r_2}) / (\delta_{r_1,r_2})$ is a scale factor to account for the variation in cardiac size based on the distance between AA and DA. The graphs in Fig. 11 show the

positive correlation between the approximate size of the heart by measuring the distance of OPs of the coronary arteries and the distance between AA and DA.

The following shape prior is modeled for the cross-sectional diameter of coronary arteries:

$$L(t_{i,z}) = -\frac{|1 - \phi_i(p)/M|^2}{\sigma_M^2} \quad (5)$$

where $M = \max \phi_i$ and $p \in t_i$. This value approaches zero for a perfect match to the model. The free parameter σ_M in Eq. (5) is the standard deviation of the size ratio, which is set to 0.1 for our implementation. We have mapped the probability values for all regions to see how the probability values change in the Section 3.2.

The coronary arteries are estimated by the following equation derived from Eq. (1):

$$\begin{aligned} \operatorname{argmax}_i P(t_i | I, \mathcal{R}) &= \operatorname{argmax}_i L(t_i | I, \mathcal{R}) = \operatorname{argmax}_i \sum_{z=1}^{N_z} \{L(I|t_{i,z}) \\ &+ \sum_{j=1}^{N_R} L(r_j|t_{i,z}) + L(t_{i,z})\} \end{aligned} \quad (6)$$

where $t_i \subseteq \mathbb{R}^3$ and $t_i = \bigcup_{z=1}^{N_z} t_{i,z}$.

Overall, the target object t_* is identified by considering the size of the coronary artery, the geometric relationship, and the attenuation of the contrast agent for all 3D candidate objects maximizing the proposed formula in Eq. (6).

Let t_*^{OP} be OP of t_* , and $* = \{RCA, LAD, LCX\}$. Then, t_*^{OP} is found by computing only geometric relations using $L(\mathcal{R}|t_{*,z})$ in Eq. (4). The OP is defined by the z -position of the target object as described in Fig. 10.

$$\begin{aligned} & \operatorname{argmax}_z L(r_{AA}, r_{DA} | t_{*,z}) \\ & = \operatorname{argmax}_z \left\{ \frac{|\mu_{r_{AA},t_{*,z}} - \lambda \cdot \delta_{r_{AA},t_{*,z}}|^2}{\sigma_{r_{AA},t_*}^2} + \frac{|\mu_{r_{DA},t_{*,z}} - \lambda \cdot \delta_{r_{DA},t_{*,z}}|^2}{\sigma_{r_{DA},t_*}^2} \right\} \end{aligned} \quad (7)$$

where AA and DA are two references defined in the Section 2.1, and the optimal parameters for μ and σ are given in Table 1. t_*^{OP} would be the target t_* at the estimated position \hat{z} by computing Eq. (7).

2.4. Grouping of vessel-like segments

The region of a coronary artery segment t_* may be a part of or close to the entire coronary artery segment. There may exist some segments that are part of a single blood vessel but are labeled separately because of plaques, noise, or motion in vessels. The eight segments labeled separately (Fig. 6(b)) will be reconnected and grouped into three segments (Fig. 6(c)) to have the same labels as

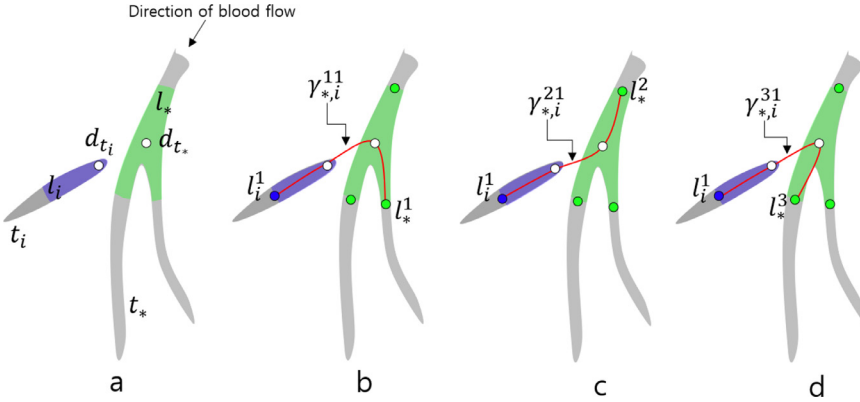


Fig. 7. The data points (blue, green) and three curves (red) connecting two segments t_* and t_i : two points, d_{t_*} and d_{t_i} , close to each other from two segments, and the local regions l^* (green shade) and l_i (blue shade) are shown in (a). The blood path in the coronary artery is more natural in (c) than in (b, d). In this example, one inlet l_i^2 and three outlets l_i^1 , l_i^2 , l_i^3 exist. There is a unique path $\gamma_{*,i}^{21}$ between t_* and t_i , and $\gamma_{*,i}^{21}$ have smaller curvature or torsion values than other curves. (For interpretation of the references to color in this figure legend, the reader is referred to the web version of this article.)

the original (Fig. 6(a)). In a similar approach [12] pairing two components, only an angle penalty between two representative tangent vectors was used. It has been demonstrated that higher-order properties of the 3D vessel trajectory are useful for an optimization method [10]. Geometric properties between segment t_* and another segment t_i are analyzed as well in order to group them together within a specific distance of 12 mm, which is a bit longer than the cut-off value of non-complex lesion length [26].

Coronary arteries are smoothly curved so that blood flows smoothly, so we assumed that the deviation of the geometric properties existing in the entire range of coronary arteries is small. We extract and utilize higher-order properties such as curvature and torsion from the 3D curves between two objects to connect and group the segments of the same coronary artery and not to connect unrelated segments such as false positives, as described in Fig. 6. Every curve contained in a plane has zero torsion, and any given triplet of points always lies in a plane, which means that at least four points are needed to approximate both curvature and torsion. Curvature and torsion use derivatives of the second and third orders, which requires a cubic curve interpolating four data points (DPs). To interpolate DPs, we need to find four corresponding control points (CPs) using Eqs. (8)–(10).

Reconstructing a cubic B-spline curve γ between two segments requires basically four CPs $P = \{p_1, p_2, p_3, p_4\}$:

$$\gamma(u) = \sigma P M U = \frac{1}{6} \begin{bmatrix} p_{1,x} & p_{1,y} & p_{1,z} \\ p_{2,x} & p_{2,y} & p_{2,z} \\ p_{3,x} & p_{3,y} & p_{3,z} \\ p_{4,x} & p_{4,y} & p_{4,z} \end{bmatrix}^T \begin{bmatrix} -1 & 3 & -3 & 1 \\ 3 & -6 & 3 & 0 \\ -3 & 3 & 0 & 0 \\ 1 & 0 & 0 & 0 \end{bmatrix} \times \begin{bmatrix} u^3 \\ u^2 \\ u \\ 1 \end{bmatrix} \quad (8)$$

where $\gamma : [0, L] \rightarrow \mathbb{R}^2$ or \mathbb{R}^3 is parameterized by arc length [27]. As the shape of a curve is determined by P , it is important to find P for all curves connecting two segments. An example of all curves is shown in Fig. 7.

Four CPs in Eq. (8) are found based on four DPs $D = \{d_1, d_2, d_3, d_4\}$. To define four DPs between two segments t_* and t_i , two estimated points d_{t_*} and d_{t_i} close to each other from two vessel segments for any pair of labeled segments t_* and t_i are found, and then two local regions of interest $l_* \subset t_*$ and $l_i \subset t_i$ within a geodesic distance d_0 from d_{t_*} and d_{t_i} are respectively considered. d_0 is set to 12 mm to cover the maximum length of a non-complex plaque of the coronary artery, which can split one vessel

into two. Then, all the tips l_*^m and l_i^n from l_* and l_i are used as the DPs $D_{mn} = \{l_*^m, d_{t_*}, d_{t_i}, l_i^n\}$ that will be interpolated by finding the corresponding CPs P_{mn} .

$$u_1 = 0, u_2 = \frac{\|d_{t_*} - l_*^m\|}{S}, u_3 = u_2 + \frac{\|d_{t_i} - d_{t_*}\|}{S}, u_4 = 1$$

$$U_{mn} = \begin{bmatrix} u_1^3 & u_2^3 & u_3^3 & u_4^3 \\ u_1^2 & u_2^2 & u_3^2 & u_4^2 \\ u_1^1 & u_2^1 & u_3^1 & u_4^1 \\ 1 & 1 & 1 & 1 \end{bmatrix} \quad (9)$$

where $S = \|p_{t_*} - l_*^m\| + \|p_{t_i} - p_{t_*}\| + \|l_i^n - p_{t_i}\|$. Parameters (U_{mn}) in Eq. (9) are approximated by calculating the polygon perimeter and ratios, and then P_{mn} is found by calculating inverse matrix $(M U_{mn})^{-1}$.

$$\frac{1}{\sigma} D_{mn} (M U_{mn})^{-1} = P_{mn}$$

$$\gamma_{*,i}^{mn}(u) = \sigma P_{mn} M U \quad (10)$$

where $D_{mn} = [l_*^m \ d_{t_*} \ d_{t_i} \ l_i^n]$. The values of m and n depend on the structures of the two segments. $M \times N$ of the curves as $\gamma_{*,i}^{mn}(u) = \gamma_{l_*^m, d_{t_*}, d_{t_i}, l_i^n}^{mn}(u)$ can exist between two segments where $(1 \leq m \leq M)$ and $(1 \leq n \leq N)$. Note that the middle of the DPs is fixed to d_{t_*} and d_{t_i} , respectively. The three possible curves ($M = 3$, $N = 1$), for example, between the two segments, are visually described in Fig. 7.

The use of geodesic distance for this problem is important for considering only related vessels. The use of Euclidean distance may include unwanted curves. Fig. 8 shows the comparison of the processes of deciding DPs to see how different geodesic and Euclidean distances can be in the same case.

The curvature and torsion [27] are defined, respectively, as

$$\kappa(u) = \frac{\|\gamma'(u) \times \gamma''(u)\|}{\|\gamma'(u)\|^3},$$

$$\tau(u) = \frac{\det[\gamma'(u) \gamma''(u) \gamma'''(u)]}{\|\gamma'(u) \times \gamma''(u)\|^2} \quad (11)$$

Let $\kappa_{*,i}^{mn}(u)$ and $\tau_{*,i}^{mn}(u)$ be the curvature and torsion of $\gamma_{*,i}^{mn}(u)$ obtained by Eq. (11). The geometric properties of the cubic B-spline $\gamma_{*,i}^{mn}(u)$ can be analytically computed. The integration of $\kappa_{*,i}^{mn}(u)$ or $\tau_{*,i}^{mn}(u)$ (Eq. (12)) indicates how smooth and natural the curve connecting two vessel segments is. They are smoother if the two vessel segments are the same or more closely related, such as parent (main) and child (branch) vessels, than other artifacts or unrelated parts. The geometric consistency between two segments t_* and t_i can be measured by

$$\sigma K_{*,i}^{mn} + \nu T_{*,i}^{mn} = \sigma \int_0^L \kappa_{*,i}^{mn}(u)^2 ds + \nu \int_0^L \tau_{*,i}^{mn}(u)^2 ds \quad (12)$$

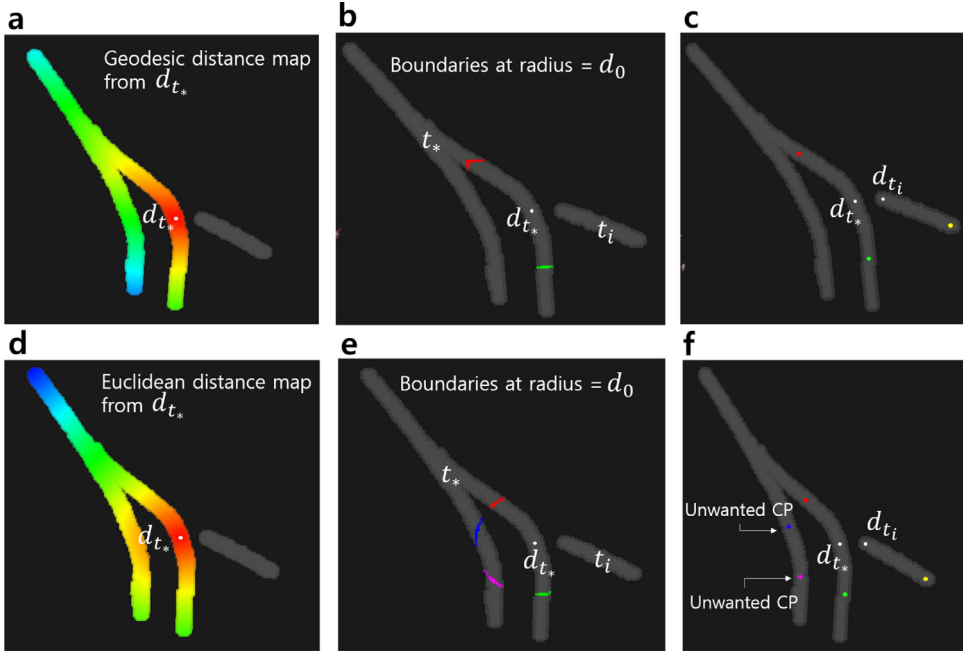


Fig. 8. Comparison between geodesic distance and Euclidean distance for deciding DPs D automatically in a synthetic case. (a) geodesic distance map from d_{t_*} , (b) labeled boundaries at the geodesic distance $d_0 = 12\text{mm}$, (c) estimated DPs, (d) Euclidean distance map from d_{t_*} , (e) labeled boundaries at Euclidean distance $d_0 = 12\text{mm}$; the boundaries on unrelated vessels are included, (f) estimated DPs with some unwanted DPs.

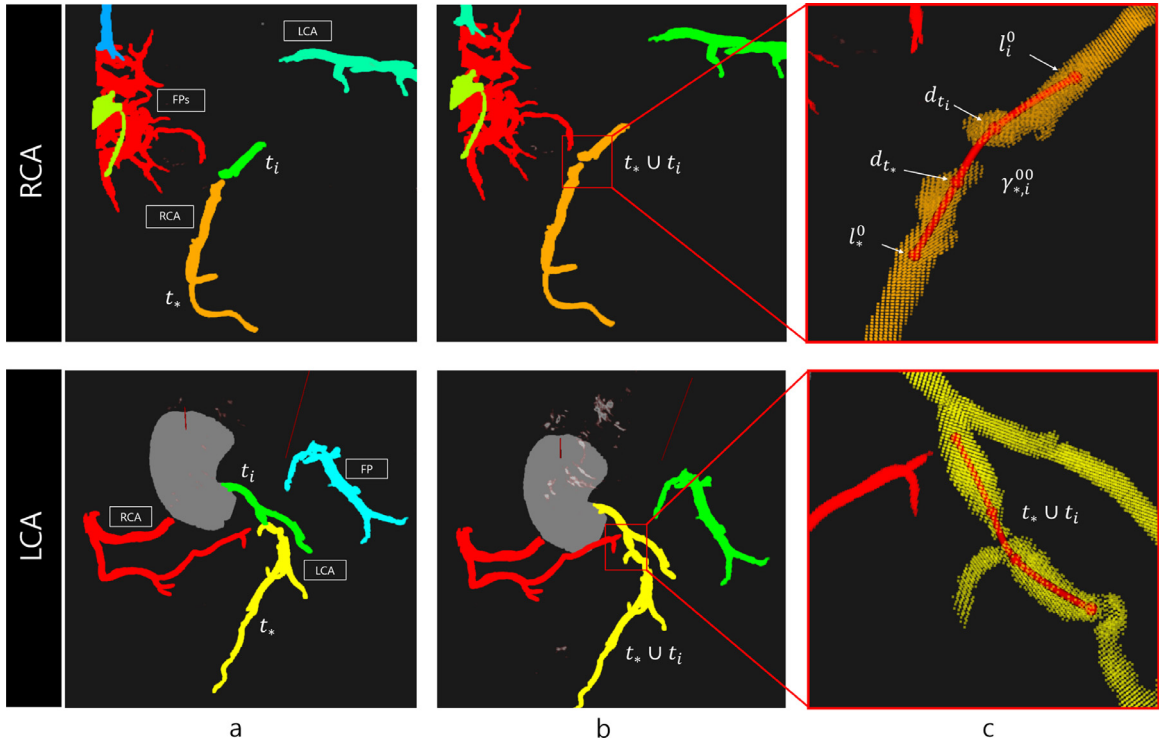


Fig. 9. Vessel segments merged by curve analysis. Both RCA and LCA (LAD + LCX) cases are presented as examples. (a) Two objects before merging. (b) The two objects merged into one. (c) The curve connecting the two objects is visualized in a magnified view.

where arc length $ds = ||\gamma'(u)||du$ and scalars σ, ν are weighting factors of curvature and torsion, respectively. The integral is approximated with numerical integration. We use the trapezoidal rule for this purpose. Then, an optimal curve with minimum curvature and torsion among $M \times N$ curves is chosen by minimizing the equation

$$\operatorname{argmin}_{m,n} \sigma K_{*,i}^{mn} + \nu T_{*,i}^{mn}. \quad (13)$$

The trajectory with the direction of blood flow in Fig. 7(c) appears to have smaller values of both curvature and torsion. From Eq. (13), an optimal curve $\gamma_{*,i}^{m_0n_0}(u)$ is estimated. We defined a simple binary operator $GR(t_*, t_i)$ that provides the value of consistency between two segments t_* and t_i by checking the geometric relation as

$$GR(t_*, t_i) = \begin{cases} 1, & \text{if } G_T \geq \sigma K_{*,i}^{m_0n_0} + \nu T_{*,i}^{m_0n_0} \\ 0, & \text{otherwise} \end{cases} \quad (14)$$

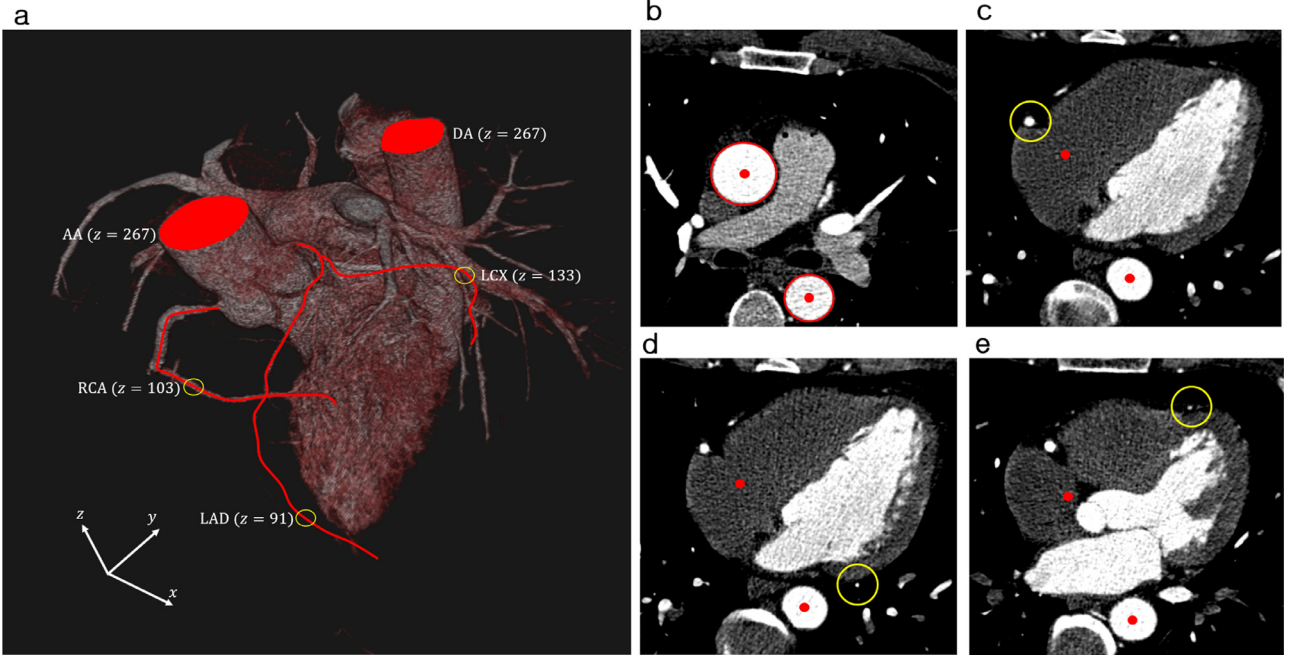


Fig. 10. Example of target annotation for the three main coronary arteries (RCA, LAD, LCX) in a 3D image based on the geometric model in Fig. 2. (a) Three OPs, two aortas (AA, DA), and centerlines of the coronary arteries are visualized in the CTA volume. The OPs of RCA, LAD, and LCX can exist on different z-axes. (b) AA (r_1) and DA (r_2) are chosen as reference objects, and they are valid for the entire range of z values using lines passing through the centroids of the aortas. (c) OP of the RCA (yellow circle) at $z = 103$; (d) OP of the LCX (yellow circle) at $z = 133$; (e) OP of the LAD (yellow circle) at $z = 91$. The annotated positions are nearly on the exterior surface of the heart. (AA, ascending aorta; CTA, computed tomography angiography; DA, descending aorta; LAD, left anterior descending artery; LCX, left circumflex artery; OP, outermost point; RCA, right coronary artery.). (For interpretation of the references to color in this figure legend, the reader is referred to the web version of this article.)

Pairs having strong connectivity are merged into one. For the parameters of Eqs. (12) and (14), σ , ν , and G_T are set to 0.7, 0.3, and 0.1, respectively. The values are chosen based on the curve analysis described in Section 3.3.

Based on the GR operator, Algorithm 1 can connect and group

Algorithm 1 Grouping vessel segments

```

1: procedure GV(initial segment set  $\mathcal{T}$ )
2:    $\psi \leftarrow 0$  // pivot index
3:    $N_\alpha \leftarrow |\mathcal{T}|$  //# of segments after merger
4:    $N_\beta \leftarrow 0$  //# of segments before merger
5:   while  $\psi < |\mathcal{T}|$  do
6:      $N_\beta \leftarrow N_\alpha$ 
7:      $t_* \leftarrow \mathcal{T}_\psi$  //pivot segment
8:     for  $i = \psi + 1$  to  $N_\beta$  do
9:       if  $GR(t_*, t_i)$  then //investigate the geometric relation-
ship
10:         $t_* \leftarrow t_* \cup t_i$  // merge two segments into one
11:         $\mathcal{T} \leftarrow \mathcal{T} \cap \mathcal{T}_i^c$  //exclude the merged one
12:      end if
13:    end for
14:     $\mathcal{T}_\psi \leftarrow t_*$  //update the pivot
15:     $N_\alpha \leftarrow |\mathcal{T}|$ 
16:    if  $N_\alpha = N_\beta$  then //shifting pivot index
17:       $\psi = \psi + 1$ 
18:    end if
19:  end while
20:  Return  $\mathcal{T}$ 
21: end procedure
```

the segments of the same coronary artery and does not connect unrelated segments. Fig. 9 shows that the coronary arteries labeled separately in a real CT image are correctly grouped by Algorithm 1. Most of the existing tracking-based approaches are automatically

terminated or leak to other organs if they are locally broken by several factors such as plaque or motion. The proposed method solves these problems with a new perspective.

3. Experiments

We performed a number of experiments to ascertain the robustness of our system and report the quantitative results for the identification of three coronary arteries in cardiac CTA images. The proposed method is compared with those used by two commercial workstations that perform fully automatic segmentation of coronary arteries. They generally extract coronary arteries automatically, but sometimes they fail during processing and require the user to provide some points manually. We also compare our results with a local geometric method (LGM) [8] for directly seeding the coronary artery. In our experiment, the cases most likely to fail are CTO cases having a long disease region and 4D (3D+t) CT images that are acquired during one cardiac cycle with motion artifacts.

3.1. Optimization of parameters of the proposed method

In order to annotate the position on the elongated coronary artery consistently, we have defined a position of the coronary artery whose variations are smaller. OP of the coronary artery is the outermost point of the coronary artery on the surface of the heart in axial view. OP is located in the middle of the coronary artery, and the length or area of the polygon consisting of the three coronary artery OPs is proportional to the size of the heart. A patient-specific cardiac scale can be defined with this property. OPs of the RCA, LAD, and LCX are annotated in CTA images, as shown in Fig. 10(a). The coronary artery is oriented in a direction stretching away from the coronary ostium that is located on the aortic surface, which has been localized based on the anatomical structure.

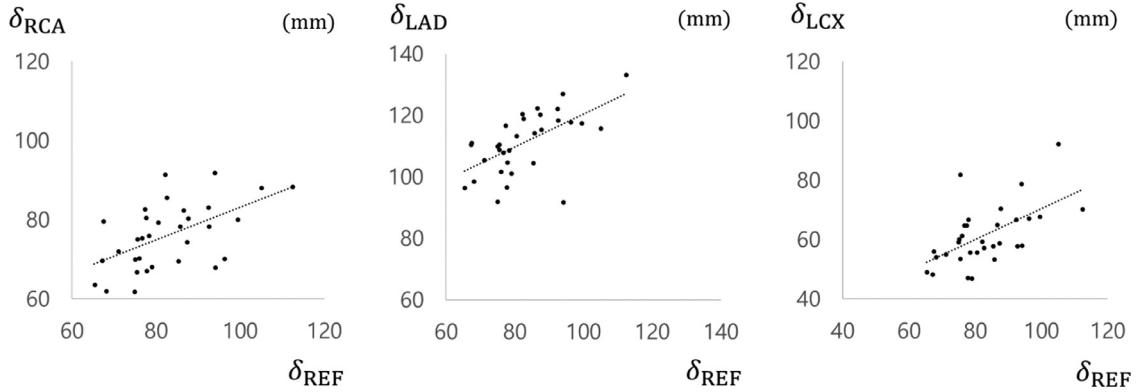


Fig. 11. The greater the distance between reference objects, the greater the size of the heart. The scatter plots show the positive correlation between the distance from AA and DA and the distance from AA or DA to the position at which the coronary artery (RCA, LAD, LCX) extends the furthest. The vertical and horizontal axes are $\delta_* = (\delta_{r_1,*} + \delta_{r_2,*})/2$ and $\delta_{\text{REF}} = \delta_{r_1,r_2}$, respectively. The positions are described in Fig. 10, and the distance-based relations among the objects are described in Fig. 2.

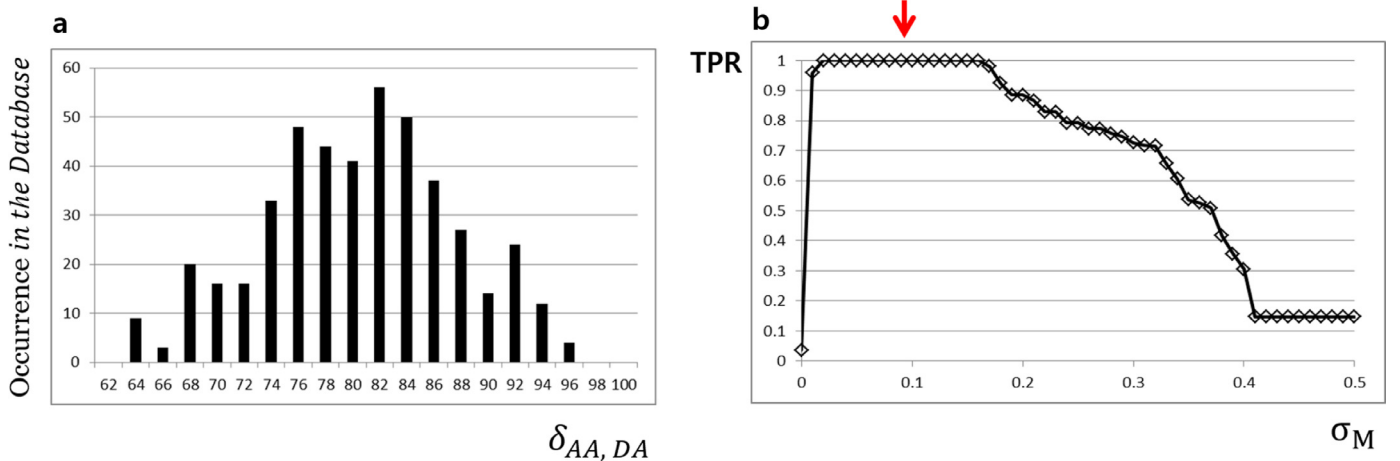


Fig. 12. (a) The distribution of the distance between reference objects (AA, DA) is seen to follow a normal distribution. (b) The true positive rate (TPR) plotted for values of the parameter σ_M in Eq. (5) while other parameters are held constant.

We annotated OPs for each coronary artery from the 32 datasets [22], and the mean μ and standard deviation σ were estimated for the prior distribution, with values as given in Table 1.

$\lambda = (\mu_{r_1,r_2})/(\delta_{r_1,r_2})$ in Eq. (4) is a ratio that is a scaling factor between mean distance μ_{r_1,r_2} estimated from ground truth (GT) data and distance δ_{r_1,r_2} measured for each case to take account of the variation in cardiac sizes. The value of λ is defined for each patient. In our problems, the values were positively correlated with the GT data, as shown in Fig. 11.

3.2. Internal parameter analysis

The stability of the system, which depends on the internal parameter values, was analyzed. In our experiments, the parameters were assumed to have normal distributions, as for the example in Fig. 12(a), and they showed such behavior in the following tests.

Although we have the parameters of prior terms estimated from the GT of the training dataset (Table 1), the weighting parameter σ_M in Eq. (5) for the likelihood function of the method is obtained experimentally. The robustness of the method for identifying coronary arteries was analyzed by varying the weighting parameter σ_M (Fig. 12(b)). The parameter was set to 0.1 in our implementation.

For the identification of coronary arteries, a coronary artery can be classified by combining the prior distributions of many vessel-like segments including non-coronary vessels near the coronary artery. Non-coronary vessels can exist very close to the target coronary artery, as shown in Fig. 13(a). They have properties very similar to those of the coronary artery in their size and contrast, so

the likelihood is not sufficient for identification in such cases, as shown in Fig. 13(b). However, they are finally classified with posterior combining the geometric priors (Fig. 13(c),(d)).

3.3. Analysis of higher-order properties for coronary artery

For objects with inconsistent structures, the deviation of these values will be very large. Based on the centerlines of the five coronary arteries obtained from the real data, the geometric values were bounded within a certain range, and in particular, torsion was almost zero from the middle to distal, as seen in the graphs of Fig. 14.

The five examples are rendered in 3D volume in Fig. 15(a)–(e). The curves in Fig. 15(c) and (d) connect the same vessel or original part, and the others (Fig. 15(a), (b), (e)) match different objects. The curves in Fig. 15(c) and (d) are assumed to be smoother and more natural than those in Fig. 15(a), (b), and (e).

We computed geometric costs based on a cubic curve γ in the domain s . Fig. 15(f) shows the integrated values of the curvatures of five curves as approximated by $\kappa(s)$. Not only do the curves between the same vessels have relatively lower curvatures, but the curve connecting false positives in Fig. 15(b) also has low curvature. The area where the small bend exists locally in Fig. 15(b) and the penalty are also slightly affected in the integrated curvature $K = \int_0^L \kappa(s)^2 ds$. However, from the torsion $\tau(s)$ in Fig. 15(g), we observe that Fig. 15(b) has steep torsion values, whereas the torsion values in Fig. 15(c) and (d) remain at approximately zero. $T = \int_0^L \tau(s)^2 ds$ representing a torsion penalty shows that the two

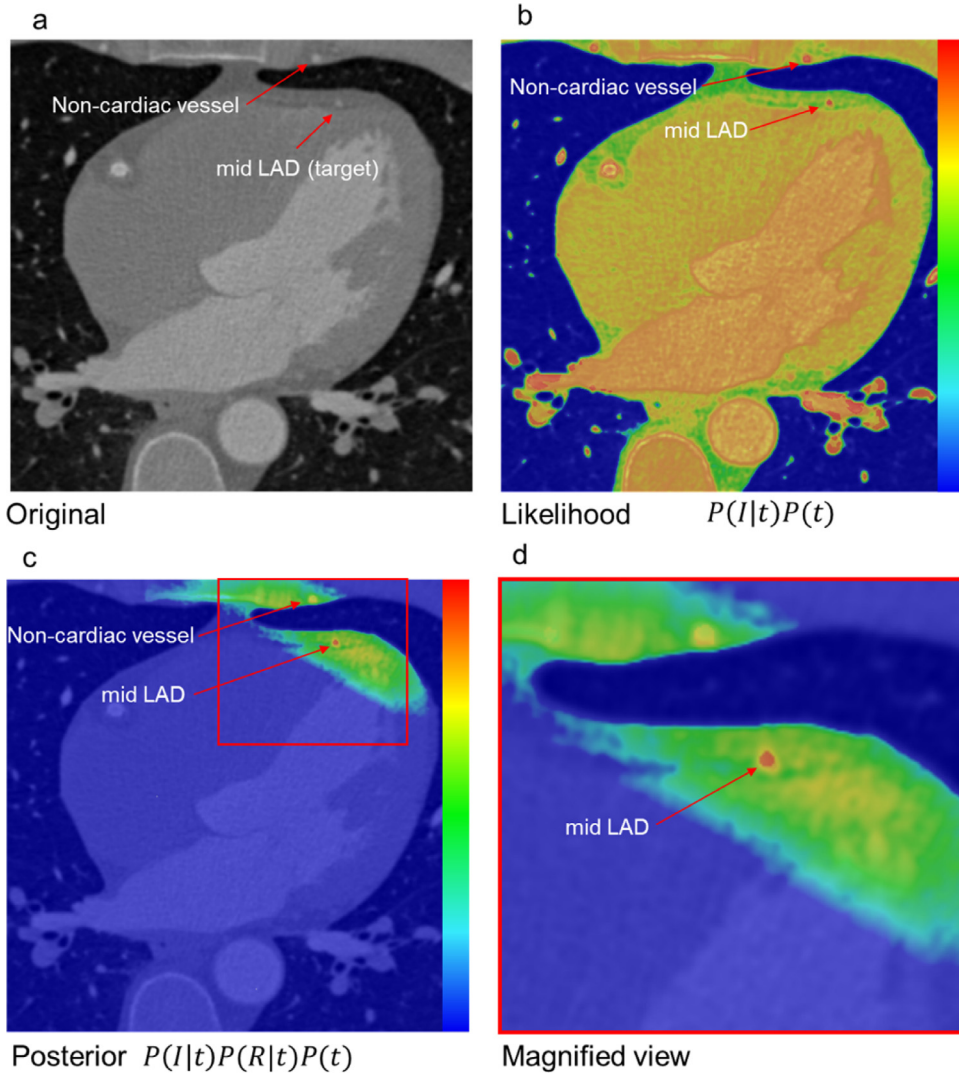


Fig. 13. An example of geometric estimation showing how a target is correctly classified around several false positive structures. (a) A 2D slice where the OPs of the LAD and another vessel exist. (b) Likelihood and prior are mapped, and two vessel-like candidates have similar potentials. (c) The false positive (FP) is penalized, and the two candidates (arrows) are clearly separated by combining the geometric priors. (d) Magnified view of the LAD area.

objects in Fig. 15(b) cannot be naturally connected. Fig. 15(a) is penalized by both terms, and for Fig. 15(e), the U-shaped curve appears almost planar with little torsion; such a U-shaped curve in this case is penalized by the curvature property. Such shapes are rarely present in coronary arteries. The cost function $\sigma K + \nu T$ comprising both properties (Fig. 15(h)) shows that the responses are lower for the real coronary artery Fig. 15(c) or the original part Fig. 15(d). Parameters σ and ν are set to 0.7 and 0.3, respectively.

3.4. Quantitative comparison with existing methods

For the quantitative evaluation, the proposed method was applied on 100 CTA cases. Thirty-two public datasets whose acquisition parameters are well defined for cardiac CTA from the Rotterdam Challenge [22,23], forty 4D (3D+t) CTA datasets, ten CTO datasets. We additionally selected 18 cases with variations in FOVs, contrast injection timings, artifacts, and morphology for our experiment. Each image was reconstructed to 512×512 pixels with a pixel size ($s_x \times s_y$) between $0.28 \text{ mm} \times 0.28 \text{ mm}$ and $0.36 \text{ mm} \times 0.36 \text{ mm}$. The number of slices varied between 296 and 422, with the slice thickness (s_z) between 0.28 mm and 0.36 mm . It should

be noted that the experiments were performed without any user interaction or parameter changes.

3.4.1. Comparison with the local geometric feature method

Some approaches for directly seeding in the middle of the coronary artery have been introduced for robust tracking in CTO cases [7,8]. Some coronary arteries are seemingly disconnected, which is the most challenging type of case for tracking methods. The local geometric method (LGM) approach [8] based on 2D local features first chooses a z-slice where coronary arteries are expected to exist. Then, heart regions are detected by 2D ray casting and ellipse fitting. In the ellipse region, via edge detection, morphological opening operation, contour tracing, and geometric analysis, local coronary ROIs are finally extracted. A Hessian-based vesselness filter is applied to select the correct objects from many 2D candidates. However, the Hessian filter does not eliminate all false positives, since the method uses only 2D local geometry. For example, many vessel-like objects exist in the left and right ventricles owing to the presence of papillary muscles. The method may need an additional process to classify the correct objects among the many vessel-like objects, which is not a simple process when only local features are used.

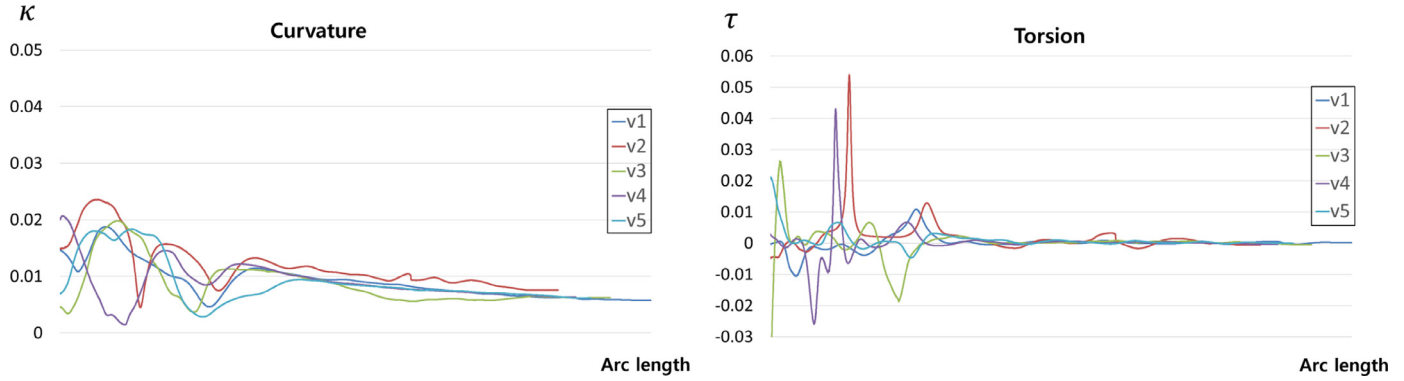


Fig. 14. The curvatures and torsions of five coronary arteries from real data. The geometric properties are found by computing Eq. (11) along the coronary centerlines [22]. Both curvature and torsion values on coronary arteries are bounded, and curves that may exist outside the boundary can be seen as structures that are not related to coronary arteries.

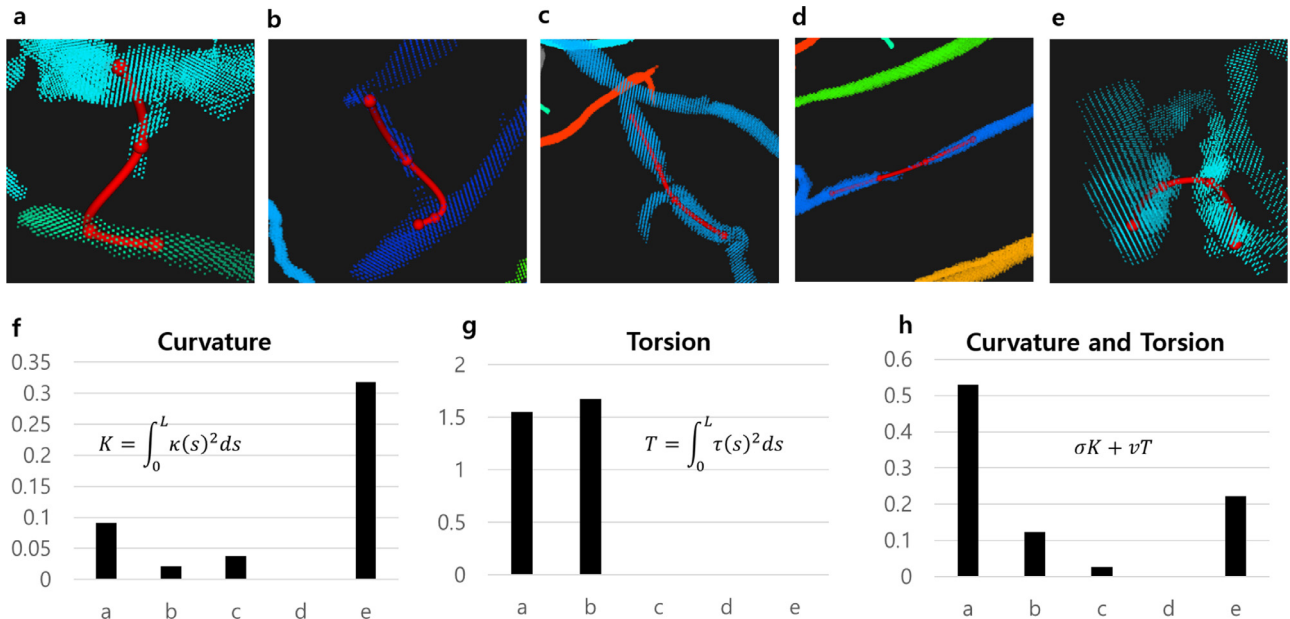


Fig. 15. Analysis of cubic curves relating two candidate objects. Five possible examples (a)–(e) of segments and connecting curves (red) are rendered in 3D space from real data. (f) and (g) show the integrated curvature and torsion values with the domain curves (a)–(e), respectively, for each curve. In (h), the final geometric values to penalize the curves unnaturally connecting two objects are plotted. (For interpretation of the references to color in this figure legend, the reader is referred to the web version of this article.)

LGM is comparable with the proposed method in terms of selecting the coronary arteries from among all the vessel-like candidates. We implemented a highly optimized LGM and compared our method with it. Fig. 16 shows the processes of the LGM (2D) and of the proposed method (3D) for identifying coronary arteries. The results by LGM include some false positives with the coronary arteries, and one coronary artery was missed. The detailed quantitative results are included in Section 3.4.3.

3.4.2. Chronic total occlusion and 4D (3D+t) cases

CTO is a disease in which the coronary artery is totally occluded by plaques, which is a challenging case for coronary artery tracking. Seemingly disconnected CTO regions, such as those shown in Fig. 17(a), have dramatic intensity changes. Along the centerline of the coronary artery, the intensity level first has the contrast shown in Fig. 17(c), which then becomes sharply lower at the initial region of CTO and remains low for a time, returning sharply to the contrast intensity again at the end of the disease region.

4D (3D+t) cases have motion artifacts, and the intensity distribution in the region with maximum coronary motion may appear momentarily weak (Fig. 17(f)). Tracking-based methods may be di-

verted to other organs having similar intensity and fail when faced with areas with disease or weak contrast, since they search locally for the next state. The results provided by a commercial workstation [28] include only the initial region near the coronary ostia (Fig. 17(b),(e)). Global-optimization-based approaches, such as [9–11], are known to be robust to such CTO cases, but they need at least two points in the proximal and distal regions. The proposed method can robustly detect the coronary region in spite of the weak regions (Fig. 17(a),(d)) for two reasons. First, the proposed method directly finds the middle of the coronary artery, since the annotated location of the prior distribution is given by the OP (Fig. 10). Second, curve analysis is performed for the two disconnected regions so that they have already been merged (Fig. 15).

The proposed method was compared with other methods in terms of robustness on ten CTO cases and four 4D cases. Two workstations found the coronary arteries with the seed point at the coronary ostia connected to the aorta. Those methods stopped at the occluded region, and then user interaction for one point immediately after the occluded region was needed to find the next regions, whereas the proposed method found the middle and dis-

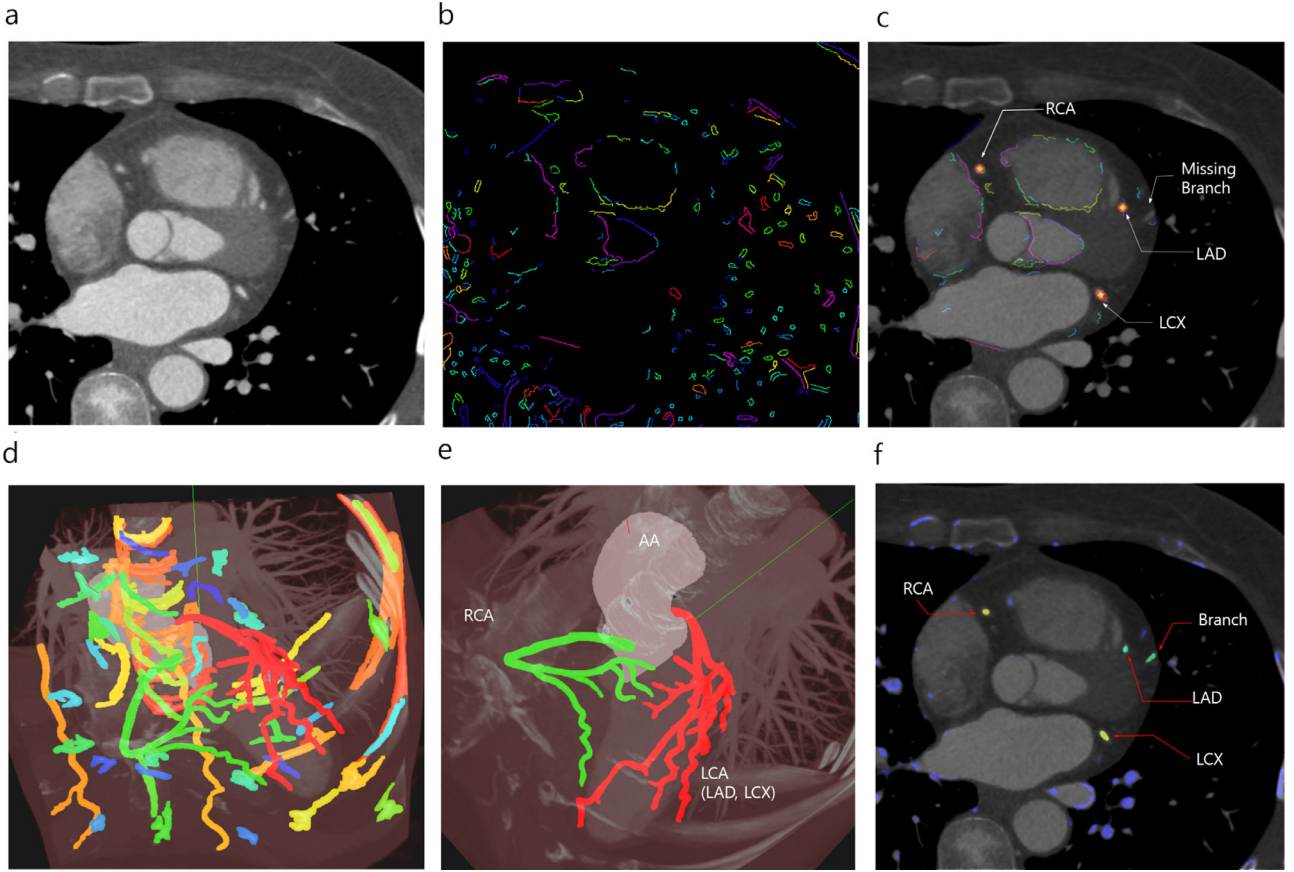


Fig. 16. The proposed method is compared with the local geometric method (LGM). LGM: (a) a selected slice in which three coronary arteries exist at $z = 170$; (b) 2D labeled edge candidates; (c) results after applying region of interest, length, and curvature constraints, including some false positives (FPs) with the true positives (TPs). With LGM, one branch was missed. Proposed method: (d) all of the 3D vessel-like candidates; (e) results in volume. All of the coronary arteries were clearly identified from among the many candidates. (f) Result of the proposed method overlaid on the same slice as (c) for comparison. With the proposed method, every coronary artery existing in the slice was found.

Table 2
Quantitative comparison of error and similarity for identification of coronary artery.

Dataset (n)		Solver			
		Proposed	QAngioCT [28]	Vitre [29]	LGM [8]
HD (error)	Public (32)	0.84 ± 0.36	0.84 ± 0.39	1.08 ± 0.59	1.74 ± 0.57
	4D (40)	0.85 ± 0.43	1.11 ± 0.42	3.07 ± 0.62	1.92 ± 0.77
	CTO (10)	1.07 ± 0.33	1.14 ± 0.27	2.33 ± 0.47	1.07 ± 0.62
	Selected (18)	0.83 ± 0.40	0.87 ± 0.37	0.92 ± 0.54	1.27 ± 0.49
JI (similarity)	Public (32)	0.68 ± 0.12	0.66 ± 0.13	0.64 ± 0.18	0.58 ± 0.21
	4D (40)	0.67 ± 0.14	0.63 ± 0.14	0.57 ± 0.22	0.43 ± 0.17
	CTO (10)	0.59 ± 0.21	0.57 ± 0.16	0.42 ± 0.24	0.46 ± 0.20
	Selected (18)	0.73 ± 0.14	0.69 ± 0.13	0.66 ± 0.17	0.58 ± 0.20

All the methods are compared with the same dataset, 100 CT images. HD: a measure, Hausdorff distance (error); The smaller value, the better. JI: a measure, Jaccard index (similarity); The larger value, the better.

tal regions directly. Details of the quantitative results are shown in the next section.

3.4.3. Statistical evaluation

Tables 2 and **3** present the results of identification of the coronary artery, a quantitative comparison of our method with the results given by two workstations (Vitre, by Vital Images [29], and QAngio CT, by Medis [28]) and LGM by a 2D local feature approach [8]. We use three measures to evaluate the robustness and accuracy:

- JI : Jaccard index, $\frac{TP}{(TP+FP+FN)}$
- HD (mm): Hausdorff distance, $\max\{\sup_{x \in X} \inf_{y \in Y} d(x, y), \sup_{y \in Y} \inf_{x \in X} d(x, y)\}$

- TPR: true positive rate, $\frac{TP}{(TP+FN)}$

where X and Y can be the outputs by one of algorithms and ground truth (GT), and values of TP, FP, and FN are defined as $TP := |x \in Y|$, $FP := |x \notin Y|$ and $FN := |Y| - |x \in Y|$, respectively. Then, JI, HD, and TPR are computed to compare the robustness and accuracy shown in **Tables 2** and **3**.

In terms of accuracy, JI and HD are used to measure the pixel-wise overlap and error based on outputs by one of the algorithms and GT. The proposed method and QAngioCT apparently depend on vesselness responses [13] for segmenting regions, which is why there is no significant difference in both JI and HD between them. On the other hand, Vitre has some cases where the detected regions invade other organs beyond the border of the blood ves-

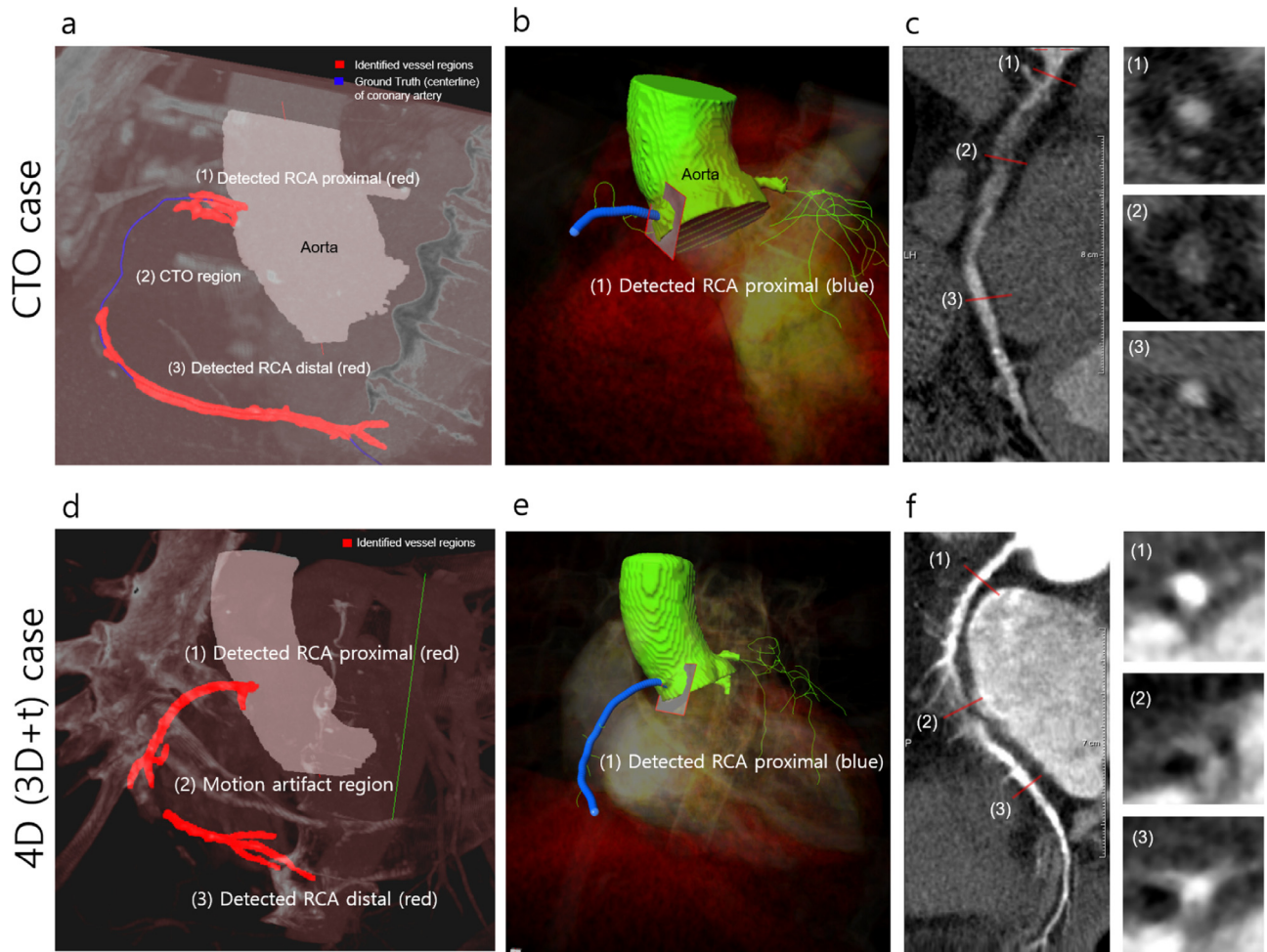


Fig. 17. CTO and 4D CTA cases using the proposed and existing methods. CTO case: (a) The proposed method directly identifies both the proximal and distal regions (red) of RCA. GT (centerline) is also shown for reference (blue). (b) the result (blue) given by the workstation [28] on the same case provides only the part before the CTO region. The lesion exists over a long area, causing tracking methods to fail; (c) curved planar reformation images and the cross-sections based on the GT. The regions (1)–(3) show how the intensity changes. 4D case: (d) the result (red) given by the proposed method. The distal part is identified after the small gap. (e) the result (blue) given by the workstation provides only the part before the motion artifact region. (f) curved planar reformation images and the cross-sections based on the GT. The regions (1)–(3) show how the intensity changes. (For interpretation of the references to color in this figure legend, the reader is referred to the web version of this article.)

Table 3

Quantitative comparison of detection rate of each coronary artery from 100 CT images: TPR is used for measurement.

	Solver	TPR			
		Proposed	QAngioCT [28]	Vitrean [29]	LGM [8]
RCA	1.00	0.90	0.94	0.82	
LAD	0.94	0.86	0.87	0.76	
LCX	0.96	0.86	0.83	0.72	
LCA	0.96	0.87	0.91	0.76	

TPR: a measure, true positive rate; The larger value, the better; RCA, right coronary artery; LAD, left anterior descending coronary artery; LCX, left circumflex artery; LCA, left coronary artery ($LAD \cup LCX$)

sels. Coronary regions detected by Vitrea also tend to be relatively larger than regions detected by other methods in our experiment. For the LGM approach, we approximate the vessel radiiuses from the detected edges to compare with other methods. LGM has a limitation that it uses only 2D local features and does not provide clear regions of the coronary artery. Overall, the result in Fig. 2 shows that the proposed method outperforms the other methods in JI and HD. The proposed method robustly detects coronary arteries in both cases with and without plaques.

For the identification problem of coronary arteries, the detection rate is very important. We measured true positive rate (TPR) for each coronary artery (RCA, LAD, LCX, and LCA) in terms of the detection rate. LCA is included in Table 3 because LAD and LCX are anatomically connected. TP for LCA increases when one of two coronary arteries is detected. The result in Table 3 shows significantly higher detection rate with the proposed method compared to the other existing methods. Vitrea is robust for detecting main coronary arteries, but it does not detect and provide small branches. QAngioCT detects not only main coronary arteries but also small branches. It sometimes failed with the disconnected coronary artery due to severe plaques or motion artifacts. LGM detects both main coronary arteries and branches among all the 2D vessel-like candidates, but compared to other methods, the number of FPs was higher, since it probably considers only 2D local features. Some cases in the CTO and 4D dataset failed under all methods because of severe plaques or motion artifacts of RCA. On the other hand, the proposed method successfully detected coronary arteries including branches even in the cases with the presence of lesions. The reconnection process of the disconnected coronary arteries made it identify the missing regions, which increases TPR for the proposed method.

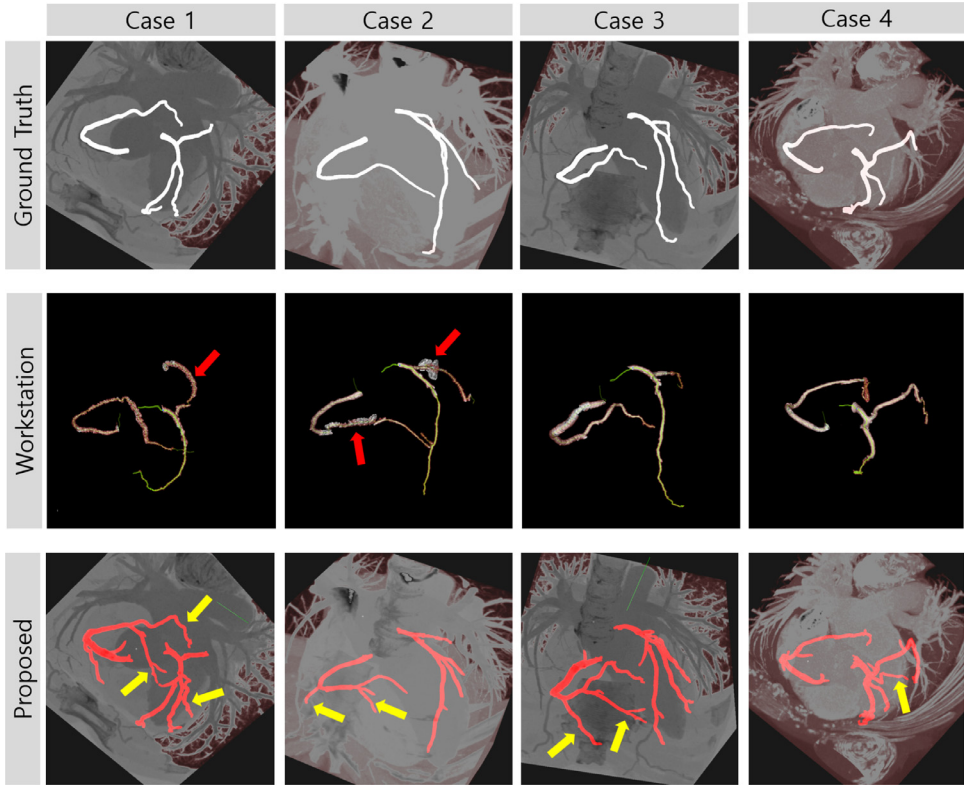


Fig. 18. Qualitative comparison: each ground truth image provided in the public dataset has a fixed number of vessels (four); each result with some misdetections (red arrow) from the workstation [29] has only three vessels, even though more vessels actually exist. Results from the proposed method bring out more vessels (yellow arrow), and the number of blood vessels matching the GT is greater than that in the results from the commercial workstation. (For interpretation of the references to color in this figure legend, the reader is referred to the web version of this article.)

Missing cases from the proposed method arose when only the part of coronary artery had very weak contrast, but such cases were challenging for all the methods. Adaptive parameter tuning is needed for the weak or non-contrast images when preparing the candidates, since our method requires candidates, and coronary motion correction methods such as [30] are expected to improve our method for 4D cases.

As a qualitative comparison in Fig. 18, the proposed method brings out more vessels, and number of blood vessels matching the GT is greater than that in the results from the commercial workstation. Our proposed method requires a total of 37–53 s computation times for the identification of coronary artery, respectively, depending on the number of z-slices with a core i7 3.50-GHz 32GB PC. The performance could be considerably improved through GPU-based parallel processing.

4. Discussion and conclusion

In this paper, we have proposed a method for robust target detection using anatomic and geometric relations among parts of the heart in cardiac CTA images via the problem, viz., identification of the coronary arteries. The method is based on the assumption that there are geometrical relationships between the anatomically defined parts and that their variation follows certain statistics. Two aortas located in the center of the heart are important objects as large pillars within the heart and serve to estimate the target. Many methods for automatic localization of the aorta have been proposed and can easily provide their locations robustly. Using two robustly detected reference locations, coronary arteries whose structures are complex can be robustly detected.

The problem of the extraction of 3D coronary arteries is still under study. Tracking-based methods are relatively fast, but if they

encounter a structure with lesions such as broken blood vessels, they may be diverted to another area or stop tracking. In addition, they are not easy to generalize because of the large variations in shape and structure in the branching area. Optimization-based algorithms to overcome the problems of tracking-based methods are known to be relatively accurate. However, it is necessary to provide manual seed points. It takes a long time to find one vessel and requires a large amount of memory.

In our newly composed method, all of the objects that can be considered as blood vessels in the CTA image are labeled as candidates, and the relations between the candidates are geometrically analyzed and merged. Main vessels and branch vessels are treated the same (without distinction) in this step. The correct coronary artery is finally selected by a Bayesian posterior considering the geometric relations. This approach avoids the challenging issues mentioned above that hinder both the tracking- and optimization-based methods.

A limitation of this method may arise when the target parts are abnormally positioned, since it uses the geometric prior distribution. Cardiac malpositions are very rarely reported, but the position of the heart can be reversed, or parts may be missing, as in cases of situs inversus, asplenia, or polysplenia. In such cases, coronary arteries may also be reversed or may not exist. The targets must be included in the estimation candidate set. The Hessian-based vesselness filter is used widely and is robust, but if the overall intensity values of the coronary arteries are too low and are difficult to distinguish from the intensity values of the surrounding muscles, the coronary artery may not get included in the candidate set.

A method for extracting a clinically optimal centerline and precisely detecting the coronary artery boundary based on the coronary artery region obtained from the proposed method should be further investigated. The methods [31,32] can detect all the land-

marks, such as the branching and end points, in the limited search space, and the vessel regions provided by the proposed method. The optimized centerlines among the landmarks can be found by the approaches [10,11,33–35].

The geometric prior distribution proposed in this paper will be applicable for any other methods that are related to the detection or segmentation of human organs if we can robustly define reference objects. Furthermore, we plan to model the heart's motion from 4D (3D+t) CT images based on the morphometric analysis to use 4D coronary artery segmentation, which would be useful to clinical fields. Also, the coronary artery segmentation method can be utilized in various clinical applications. One of clinical applications is a 2D/3D information fusion by registration of two coronary artery geometries from 2D X-ray and 3D CT images for guiding coronary artery stent procedures such as the methods [36–38]. Moreover, the proposed method can be applied to generate computational geometries for use in an image-based simulation framework, such as the methods [39–41].

Acknowledgment

This research was supported by the Leading Foreign Research Institute Recruitment Program through the [National Research Foundation of Korea](#) funded by the Ministry of Science, ICT & Future Planning (No. [2012027176](#)).

Supplementary material

Supplementary material associated with this article can be found, in the online version, at doi:[10.1016/j.patcog.2019.07.003](https://doi.org/10.1016/j.patcog.2019.07.003)

References

- [1] A.D. Lopez, C.D. Mathers, M. Ezzati, D.T. Jamison, C.J. Murray, Global and regional burden of disease and risk factors, 2001: systematic analysis of population health data, *Lancet* 367 (9524) (2006) 1747–1757.
- [2] G. Yang, P. Kitslaar, M. Frenay, A. Broersen, M.J. Boogers, J.J. Bax, J.H. Reiber, J. Dijkstra, Automatic centerline extraction of coronary arteries in coronary computed tomographic angiography, *Int. J. Cardiovasc. Imaging* 28 (4) (2012) 921–933.
- [3] Y. Zheng, H. Tek, G. Funka-Lea, S.K. Zhou, F. Vega-Higuera, D. Comaniciu, Efficient detection of native and bypass coronary ostia in cardiac CT volumes: Anatomical vs. pathological structures, in: International Conference on Medical Image Computing and Computer-Assisted Intervention, Springer, 2011, pp. 403–410.
- [4] C. Wang, O. Smedby, An automatic seeding method for coronary artery segmentation and skeletonization in CTA, *Insight J.* 43 (2008) 1–8.
- [5] Y. Zheng, H. Tek, G. Funka-Lea, Robust and accurate coronary artery centerline extraction in CTA by combining model-driven and data-driven approaches, in: Medical Image Computing and Computer-Assisted Intervention—MICCAI 2013, Springer, 2013, pp. 74–81.
- [6] M.A. Gülsün, G. Funka-Lea, P. Sharma, S. Rapaka, Y. Zheng, Coronary centerline extraction via optimal flow paths and CNN path pruning, in: International Conference on Medical Image Computing and Computer-Assisted Intervention, Springer, 2016, pp. 317–325.
- [7] M.M. Jawaid, R. Rajani, P. Liatsis, C.C. Reyes-Aldasoro, G. Slabaugh, A hybrid energy model for region based curve evolution-application to CTA coronary segmentation, *Comput. Methods Programs Biomed.* 144 (2017) 189–202.
- [8] D. Han, N.-T. Doan, H. Shim, B. Jeon, H. Lee, Y. Hong, H.-J. Chang, A fast seed detection using local geometrical feature for automatic tracking of coronary arteries in cta, *Comput. Methods Programs Biomed.* 117 (2) (2014) 179–188.
- [9] C. Metz, M. Schaap, A. Weustink, N. Mollet, T. van Walsum, W. Niessen, Coronary centerline extraction from CT coronary angiography images using a minimum cost path approach, *Med. Phys.* 36 (12) (2009) 5568–5579.
- [10] J. Ulén, P. Strandmark, F. Kahl, Shortest paths with higher-order regularization, *IEEE Trans. Pattern Anal. Mach. Intell.* 37 (12) (2015) 2588–2600.
- [11] W. Liao, S. Wörz, C.-K. Kang, Z.-H. Cho, K. Rohr, Progressive minimal path method for segmentation of 2D and 3D line structures, *IEEE Trans. Pattern Anal. Mach. Intell.* 40 (3) (2018) 696–709.
- [12] A. Szymczak, A. Stillman, A. Tannenbaum, K. Mischaikow, Coronary vessel trees from 3d imagery: a topological approach, *Med. Image Anal.* 10 (2006) 548–559.
- [13] A.F. Frangi, W.J. Niessen, K.L. Vincken, M.A. Viergever, Multiscale vessel enhancement filtering, in: International Conference on Medical Image Computing and Computer-Assisted Intervention, Springer, 1998, pp. 130–137.
- [14] O. Merveille, H. Talbot, L. Najman, N. Passat, Curvilinear structure analysis by ranking the orientation responses of path operators, *IEEE Trans. Pattern Anal. Mach. Intell.* 40 (2) (2018) 304–317.
- [15] P. Bibiloni, M. González-Hidalgo, S. Massonet, A survey on curvilinear object segmentation in multiple applications, *Pattern Recognit.* 60 (2016) 949–970.
- [16] D. Palti-Wasserman, A.M. Bruckstein, R.P. Beyar, Identifying and tracking a guide wire in the coronary arteries during angioplasty from x-ray images, *IEEE Trans. Biomed. Eng.* 44 (2) (1997) 152–164.
- [17] R. Stoica, X. Descombes, J. Zerubia, A Gibbs point process for road extraction from remotely sensed images, *Int. J. Comput. Vis.* 55 (2) (2004) 121–136.
- [18] Q. Zou, Y. Cao, Q. Li, Q. Mao, S. Wang, Cracktree: automatic crack detection from pavement images, *Pattern Recognit. Lett.* 33 (3) (2012) 227–238.
- [19] N. Batool, R. Chellappa, Fast detection of facial wrinkles based on Gabor features using image morphology and geometric constraints, *Pattern Recognit.* 48 (3) (2015) 642–658.
- [20] B. Jeon, Y. Hong, D. Han, Y. Jang, S. Jung, Y. Hong, S. Ha, H. Shim, H.-J. Chang, Maximum a posteriori estimation method for aorta localization and coronary seed identification, *Pattern Recognit.* 68 (2017) 222–232.
- [21] S. Pfaffenberger, P. Bartko, A. Graf, E. Pernicka, J. Babayev, E. Lolic, D. Bonderman, H. Baumgartner, G. Maurer, J. Mascherbauer, Size matters!: impact of age, gender, height, and weight on the normal heart size, *Circulation* (2013). CIRCIMAGING-113
- [22] M. Schaap, C.T. Metz, T. van Walsum, A.G. van der Giessen, A.C. Weustink, N.R. Mollet, C. Bauer, H. Bogunović, C. Castro, X. Deng, et al., Standardized evaluation methodology and reference database for evaluating coronary artery centerline extraction algorithms, *Med. Image Anal.* 13 (5) (2009) 701–714.
- [23] Rotterdam coronary artery challenge 2008, (<http://coronary.bigr.nl/centerlines/>).
- [24] Y. Jang, H.Y. Jung, Y. Hong, I. Cho, H. Shim, H.-J. Chang, Geodesic distance algorithm for extracting the ascending aorta from 3D CT images, *Comput. Math. Methods Med.* 2016 (2016).
- [25] O.C. Avila-Montes, U. Kurkure, R. Nakazato, D.S. Berman, D. Dey, I.A. Kakadiaris, Segmentation of the thoracic aorta in noncontrast cardiac CT images, *IEEE J. Biomed. Health Inform.* 17 (5) (2013) 936–949.
- [26] A. Alghamdi, M. Balgaith, A. Alkhaldi, Influence of the length of coronary artery lesions on fractional flow reserve across intermediate coronary obstruction, *Eur. Heart J. Suppl.* 16 (suppl_B) (2014) B76–B79.
- [27] A.N. Pressley, Elementary Differential Geometry, Springer Science & Business Media, 2010.
- [28] Medis, (<https://www.medis.nl/>).
- [29] Vital, (<https://www.vitalimages.com/>).
- [30] R. Bhagalia, J.D. Pack, J.V. Miller, M. Iatrou, Nonrigid registration-based coronary artery motion correction for cardiac computed tomography, *Med. Phys.* 39 (7Part1) (2012) 4245–4254.
- [31] M. Liu, R. Gong, W. Chen, H. Peng, 3D neuron tip detection in volumetric microscopy images using an adaptive ray-shooting model, *Pattern Recognit.* 75 (2018) 263–271.
- [32] F. Grélard, F. Baldacci, A. Vialard, J.-P. Domenger, New methods for the geometrical analysis of tubular organs, *Med. Image Anal.* 42 (2017) 89–101.
- [33] K. Lidayova, H. Frimmel, C. Wang, E. Bengtsson, Ö. Smedby, Fast vascular skeleton extraction algorithm, *Pattern Recognit. Lett.* 76 (2016) 67–75.
- [34] A. Sironi, E. Türetken, V. Lepetit, P. Fua, Multiscale centerline detection, *IEEE Trans. Pattern Anal. Mach. Intell.* 38 (7) (2016) 1327–1341.
- [35] B. Kerautret, A. Krähenbühl, I. Deblé-Rennesson, J.-O. Lachaud, Centerline detection on partial mesh scans by confidence vote in accumulation map, in: Pattern Recognition (ICPR), 2016 23rd International Conference on, IEEE, 2016, pp. 1376–1381.
- [36] D. Rivest-Henault, H. Sundar, M. Cheriet, Nonrigid 2d/3d registration of coronary artery models with live fluoroscopy for guidance of cardiac interventions, *IEEE Trans. Med. Imaging* 31 (8) (2012) 1557–1572.
- [37] W. Yu, M. Tannast, G. Zheng, Non-rigid free-form 2d–3d registration using a b-spline-based statistical deformation model, *Pattern Recognit.* 63 (2017) 689–699.
- [38] W. Xia, Q. Jin, C. Ni, Y. Wang, X. Gao, Thorax x-ray and ct interventional dataset for nonrigid 2D/3D image registration evaluation, *Med. Phys.* 45 (11) (2018) 5343–5351.
- [39] B.L. Nørgaard, J. Leipsic, S. Gaur, S. Seneviratne, B.S. Ko, H. Ito, J.M. Jensen, L. Mauri, B. De Bruyne, H. Bezerra, et al., Diagnostic performance of noninvasive fractional flow reserve derived from coronary computed tomography angiography in suspected coronary artery disease: the nxr trial (analysis of coronary blood flow using ct angiography: next steps), *J. Am. Coll. Cardiol.* 63 (12) (2014) 1145–1155.
- [40] C. Tesche, C.N. De Cecco, S. Baumann, M. Renker, T.W. McLaurin, T.M. Duguay, R.R. Bayer 2nd, D.H. Steinberg, K.L. Grant, C. Canstein, et al., Coronary ct angiography-derived fractional flow reserve: machine learning algorithm versus computational fluid dynamics modeling, *Radiology* 288 (1) (2018) 64–72.
- [41] D. Jia, B. Jeon, H.-B. Park, H.-J. Chang, L.T. Zhang, Image-based flow simulations of pre-and post-left atrial appendage closure in the left atrium, *Cardiovasc. Eng. Technol.* (2019) 1–17.



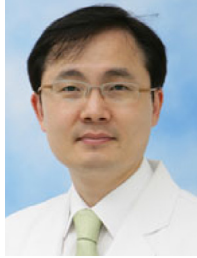
Byunghwan Jeon is with Cardiovascular ICT Research Center. He received a BS degree in computer science and engineering from Hankuk University of Foreign Studies (HUFS), and he is currently a Ph.D. candidate in medical science from Yonsei University. His research interests include medical image/signal processing, pattern recognition, and neural networks.



Hackjoon Shim received his BS degree from Seoul National University, Seoul, Korea, in 1993. He received masters degree in E. E. from Seoul National University, Seoul, Korea, in 1995. His Ph.D. from Seoul National University, Seoul, Korea, in 2007. He was a research professor from 2008 to 2010 at Seoul National University. He is currently a Research Assistant Professor of Cardiovascular ICT Research Center, Seoul, Korea. His main research interest is in object recognition, computer vision, medical image processing.



Yeonggul Jang is with Cardiovascular ICT Research Center. He received a BS degree in computer science and engineering from Hankuk University of Foreign Studies (HUFS), and he is currently a Ph.D. candidate in medical science from Yonsei University. His research interests include medical image/signal processing, pattern recognition, and neural networks.



Hyuk-Jae Chang received his MD from Yonsei University Medical School, Korea, in 1999. He received Ph.D. from Ajou University Medical School, Korea, in 2003. He is currently a Professor in Yonsei University, College of Medicine and a director of Cardiovascular ICT Research Center, Seoul, Korea. He is interested in image-based patient-specific simulation, image segmentation and quantification from multi-modality imaging and AI-based clinical decision support system.